Mon. Not. R. Astron. Soc. **000**, 1–12 (2014) Printed 31 March 2014 (MN LATEX style file v2.2)

Violating the General Density-Slope Anisotropy Inequality

Jeremy A. Barber[1⋆], Hongsheng Zhao[1]
[1] *Scottish Universities Physics Alliance, University of St Andrews, North Haugh, St Andrews, Fife, KY16 9SS, UK*

arXiv:1403.7396v1 [astro-ph.GA] 28 Mar 2014

Accepted —. Received —:

ABSTRACT
We examine the robustness of the well-known empirical relationship between the density slope and the velocity anisotropy of collisionless systems. This relation, known as the Global Density-Slope Anisotropy Inequality (GDSAI) (Ciotti & Morganti 2010), posits that no collisionless system with a globally positive distribution function exists where the anisotropy exceeds half of the power-law of the density slope. We significantly extend previous indications that the GDSAI is not a universal rule by identifying a class of models where violation occurs. These models possess a globally positive DF, have an isotropic central core, but are not guaranteed to be stable. Our analysis suggests that stability criteria provide a stronger basis for determining if a DF represents an equilibrium solution for a collisionless system.

Key words: methods: numerical, methods: analytical, galaxies: haloes

1 INTRODUCTION

The study of collisionless systems is vital to understanding structure at all scales but is often complicated by the large number of degrees of freedom in such systems. While observations of stellar clusters, galaxies, and other structures can determine some properties, it is often difficult to completely describe all properties of a particular system without some kind of external constraints or assumptions being applied.

This motivates a need to develop constraints on the permitted ranges of certain parameters such as velocity dispersions, densities, and so on. Examples of such constraints include the Jeans' Equations, which can help determine whether certain combinations of properties lead to an equilibrium system, or the more powerful constraint of requiring that the system's phase-space density is always positive.

In particular there is a demand to develop more specific limitations that significantly constrain the parameter space of collisionless systems. For example, one of the most significant recent examples is the development of the NFW (Navarro et al. 1996) profile to describe the density of all galactic dark halos. While observational limits on these halos have been improving (Clowe et al. 2006; Komatsu et al. 2009), the possibility that all halos conform to the same power-law density is extremely useful for their study.

An important step towards a general analytical constraint was made by Hansen (2004) in the form of hard constraints on the conditions in the centre of a dark halo under reasonable assumptions of spherical symmetry, a power law phase-space density (Taylor & Navarro 2001), and the requirement for physical solutions to the Jeans Equations. So, an inner density profile $\rho \propto r^{-\gamma}$ would obey $1 + \beta \leqslant \gamma \leqslant 3$ where β is the velocity anisotropy parameter.

We examine here the latest step towards developing universal constraints on spherical, collisionless systems. The work of Ciotti & Morganti (2010) is built upon several papers and includes the requirement for a non-negative distribution function (DF) (An & Evans 2006) and expansion to cover multi-component systems (Ciotti & Pellegrini 1992; Ciotti & Morganti 2009). Their result was a general result for systems that were described by Osipkov-Merritt models (Osipkov 1979) and generalised Cuddeford models (Cuddeford 1991).

$$\gamma \geqslant 2\beta \tag{1}$$

This lead to the hypothesis that Eq. 1 represented a constraint on every part of a spherical system, insofar as it was a constraint on the positivity of the DF, and was termed the Global Density-Slope Anisotropy Inequality, or 'GDSAI'. Our goal is to investigate possible violations of the inequality that would counter that proposal.

Such exceptions have already been identified in Van Hese et al. (2011) where the GDSAI was tested in systems with separable DFs. They demonstrated that the GDSAI cannot be truly universal after identifying counter-examples in systems with central cusp $\gamma_0 = 1$ and central anisotropy $\beta_0 > 1/2$. However, those systems all had significant problems with non-radial instability. Furthermore the GDSAI was still unchallenged in separable systems with $\beta_0 \leqslant 1/2$ and $\gamma_0 < 1$ and the methods proposed for more general violations were not shown to have positive DFs. All of the

⋆ E-mail: jab22@st-andrews.ac.uk (JAB); hz4@st-andrews.ac.uk (HZ)

counter-examples required extreme values for the central anisotropy and the violations, while certainly present, were of limited magnitude.

In this paper we demonstrate a simple spherical model that significantly violates the GDSAI over a range of radii. This is done with a DF that is separable in E and L^2, globally positive, and has an isotropic core. We present this as further evidence against the idea that the GDSAI applies to all spherical systems and is a simple guideline for the non-negativity of the DF. We instead suggest that, since our DF is not always dynamically stable, system stability is still the principle measure that can confirm whether a collisionless structure can be created and kept in equilibrium.

In §2 we briefly confirm the inadequacies of a purely Jeans Equation-based approach, §3 shows our construction of a simple system that violates the inequality, §4 examines the practical implications of the system, §5 examines the stability of the system, §6 describes the generalisation of our model, and §7 concludes.

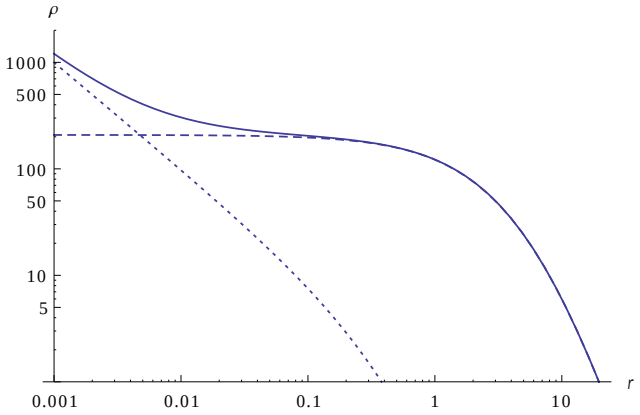

Figure 1. Density profiles of a simple composite model designed to violate the GDSAI. The dashed and dotted lines are the $1/r(1+r)^3$ cored and $5\times10^5/(7+r^4)$cusped subsidiary models while the solid line is the sum of the two profiles.

2 THE INADEQUACY OF A JEANS' EQUATION APPROACH

It is already known that the criteria provided by the Jeans' equations are not as stringent as testing for the positivity of the distribution function. However, there are mathematical difficulties associated with calculating properties of most general DF's which mean the Jeans' equations are still relevant. We will first demonstrate why apparently simple violations of the GDSAI which rely on the Jeans' equations are insufficient to disprove it, as noted in Ciotti & Morganti (2010). This is done by creating a density profile from two simple, superimposed models which, together, should apparently break the GDSAI according to the Jeans' equation. We will then show why the model fails to achieve this by being unphysical in a way that the Jeans' equations cannot indicate.

We first overlay a large cusped model from the Zhao (1996) family of models onto a smaller, cored, Hernquist model (Hernquist 1990) to create a structure that looks like Fig. 1. The system is described by:

$$\rho = \frac{1}{r(1+r)^3} + \frac{5\times10^5}{(7+r)^4} \tag{2}$$

$$\phi = -\frac{2\pi(7000147 + 8500042r + 1500003r^2}{3r(1+r)(7+r)^2} \tag{3}$$

The smaller model has a cusp with $\rho \propto r^{-1}$ in the centre transitioning to $\rho \propto r^{-4}$ while the larger of the two models is cored. This means the constant density core extends past the point where the smaller model has declined to r^{-4}. This creates a region in between the r^{-1} cusp and the r^{-4} halo where the Hernquist profile starts to dominate leading to a flattening of the density profile. In this region the density slope is very close to zero, so if we state that our system has an anisotropy of $\beta = 1/2$ everywhere then the inequality will clearly be violated in that section.

So, we then attempt to solve the Jeans' equation for the system.

$$-\frac{\mathrm{d}(\rho\sigma_r^2)}{\rho \mathrm{d}r} - \frac{2\beta\sigma_r^2}{r} = \frac{\mathrm{d}\phi}{\mathrm{d}r} \tag{4}$$

We want to solve this for σ_r^2 so it is easier to express it as the following given a constant β:

$$\rho r^{2\beta}\sigma_r^2 = \int_r^\infty \rho r^{2\beta}\frac{\mathrm{d}\phi}{\mathrm{d}r}\,\mathrm{d}r \tag{5}$$

By definition, we can replace $\frac{\mathrm{d}\phi}{\mathrm{d}r}$ with terms of density instead.

$$\rho r^{2\beta}\sigma_r^2 = \int_r^\infty \rho r^{2\beta}\frac{G}{r^2}\left[\int_0^r 4\pi r^2\rho\,\mathrm{d}r\right]\,\mathrm{d}r \tag{6}$$

A full, rigorous treatment of this integral can be performed, however the density function is sufficiently complex that the analytical result is too large to be worth reproduction here. The result is a collection of hypergeometric series which depend, in part, upon β.

The problem is that the result for σ_r^2 is not defined for all values of β. If β is such that $\beta \geqslant 1/2$ then our expression will include instances of evaluating $1/0$ which is undefined. In other words, we cannot evaluate σ_r^2 for $\beta \geqslant 1/2$ meaning that any attempt to force an anisotropy which violates the GDSAI results in an unphysical solution.

The problem is that it is difficult to predict this failure in advance of solving a specific instance of the Jeans' equation. The separate components of the model are both stable, so nothing immediately seems to be wrong with the system that we attempted to create. Rather than working through large numbers of possible models to find combinations of parameters that work, it is easier to work directly with distribution functions.

For instance, with the benefit of a little *a priori* knowledge, we could have known this system would not be physical. In a system such as this we can assume that the distribution function follows the form (An & Evans 2006; Cuddeford 1991):

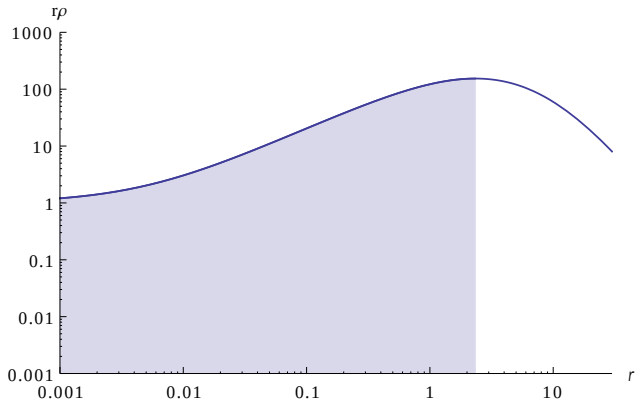

Figure 2. Plot of $r\rho$, the differential of which comprises half of the energy function of Eq. 8. As discussed in the text around Eq. 8, we require this function to have a negative gradient everywhere in order for the DF to be non-negative. This figure shows that everywhere where the model could potentially be involved in violating the GDSAI has a positive gradient, indicated by the shaded areas, strongly suggesting the model is unphysical.

$$DF_{(E,L)} = L^{-2\beta} f(E)\,;\, f(E) = -\frac{\mathrm{d}(r\rho)}{\mathrm{d}\phi} \tag{7}$$

The problem is that the angular momentum term will always be positive but if we look at the energy term there is one region where $f(E)$ is locally negative. We can see this more clearly by breaking down the expression for the energy function:

$$f(E) = -\frac{\mathrm{d}(r\rho)}{\mathrm{d}\phi} = -\frac{\mathrm{d}(r\rho)}{\mathrm{d}r} \Big/ \frac{\mathrm{d}(\phi)}{\mathrm{d}r} \tag{8}$$

To be clear, given that we need the entire energy term to be non-negative and non-zero everywhere, we require $\frac{\mathrm{d}(r\rho)}{\mathrm{d}r} / \frac{\mathrm{d}(\phi)}{\mathrm{d}r} < 0$. However, the term $\frac{\mathrm{d}(\phi)}{\mathrm{d}r}$ is always going to be positive as $\frac{\mathrm{d}(\phi)}{\mathrm{d}r} \equiv \frac{GM(<r)}{r^2}$ and clearly neither the radius nor the contained mass will be able to become negative. The problem comes from the other term, $\frac{\mathrm{d}(r\rho)}{\mathrm{d}r}$, i.e. ρ must fall steeper than r^{-1}.

The problem is highlighted in Fig. 2 where we see that $r\rho$ rises for all small radii, meaning the gradient is positive. This is the region that we are interested as it contains the transition between the two components of our model and the region in which we were trying to violate the inequality. However, since the gradient is positive here, our energy function Eq. 8 will be negative. This has the unfortunate implication that there is a significant section of our system for which the DF is negative overall; *the system is unphysical.*

In other words, the one region where we would hope to force a violation of the inequality is unphysical by definition. If we are to attempt to violate the GDSAI we are going to have to start with the DF and work up, rather than the other way around.

3 THE DISTRIBUTION FUNCTION APPROACH

We set up a system where the distribution function (DF) is defined as:

$$f(E, L) = A\delta(E - E_0)H\left(L_{cut}^2 - L^2\right) \tag{9}$$

where the constant A is for dimensional consistency. This represents a system where all allowed orbits have exactly energy E_0 and must have angular momentum L^2 of under L_{cut}^2. This is signified by the unique energy being a delta function for a particular E_0 and angular momentum being described by a *Heaviside function*:

$$H(L_{cut}^2 - L^2) = \begin{cases} 1 & \text{if } L^2 < L_{cut}^2 \\ 0 & \text{if } L^2 > L_{cut}^2 \end{cases} \tag{10}$$

This system is actually a particular type of polytropic model developed in Polyachenko et al. (2013) to study radial orbit instability. The model we use is equivalent to their $q = -1$ mono-energy model and is interesting to us for its non-monotonic density profile. Given that the DF is potentially of interest, we wish to extract density and anisotropy profiles from it to examine the point in detail.

3.1 Finding density

By definition, integrating the phase-space density (*i.e.* the DF) over all phase-space yields the mass density so we may write:

$$\rho(r) = \int f(E, L)\,\mathrm{d}v_x\,\mathrm{d}v_y\,\mathrm{d}v_z = \int f(E, L)\,\mathrm{d}v_r\,\mathrm{d}v_\theta\,\mathrm{d}v_\phi \tag{11}$$

To ease the subsequent integration we express the integration variables in terms of E and L which we do by solving only for a constant radius, r. We use the following relationships between the velocity components:

$$v_\theta^2 + v_\phi^2 = \frac{L^2}{r^2} \tag{12}$$

$$v_r = \sqrt{2\left[E - \Phi(r) - \frac{L^2}{2r^2}\right]} \tag{13}$$

These are then used to rewrite our integration variables:

$$\mathrm{d}v_r\,\mathrm{d}v_\theta\,\mathrm{d}v_\phi = \frac{\mathrm{d}E}{v_r}\,\frac{\pi}{r^2}\,\mathrm{d}L^2 \tag{14}$$

We first integrate with respect to E. This is simple as there is only one function of E, namely v_r, and the delta function which makes the integration trivial. We are then just left with the integration of L^2:

$$\rho = \frac{A\pi}{r^2}\int_0^{L_{cut}^2}\left[2\left(E_0 - \Phi - \frac{L^2}{2r^2}\right)\right]^{-\frac{1}{2}}\,\mathrm{d}L^2 \tag{15}$$

A similar trick is employed to deal with the Heaviside function as it has the property of constraining the limits of integration.We thus end up with an expression for the density:

$$\rho = 4A\sqrt{2}\pi\left(\sqrt{E_0 - \overline{\Phi}} - \sqrt{E_0 - \Phi - \frac{L_{cut}^2}{2r^2}}\right) \tag{16}$$

We note that the second square root can become imaginary for small values of r or particularly large values of L_{cut}^2. This represents parts of the system where all real orbits of the system lie under the angular momentum threshold. Consequently, the only excluded orbits are those which do not correspond to real possible states of the system. We avoid mathematical inconsistency in such cases only taking the real component of the result *i.e.* 0.

3.2 Finding anisotropy

Next we find an expression for the anisotropy. We start from the definition:

$$1 - \beta(r) = \frac{\sigma_\theta^2 + \sigma_\phi^2}{2\sigma_r^2} \tag{17}$$

Now we use the fact that $v^2\rho$ gives us the pressure along an given axis and combine it with our definition from Eq. 11. The velocity dispersion can thus be written as:

$$\sigma_r^2 = \frac{\int v_r^2 f(E,L)\,\mathrm{d}^3 v}{\rho(r)} \tag{18}$$

and likewise for $\sigma_\theta^2 = \sigma_\phi^2$.

Applying this to Eq. 17 and cancelling the factors of $\rho(r)$, noticing that symmetry tells us they are equivalent, we are left with the following:

$$1 - \beta(r) = \frac{\int \left(v_\theta^2 + v_\phi^2\right) f(E,L)\,\mathrm{d}v_r\,\mathrm{d}v_\theta\,\mathrm{d}v_\phi}{\int \left(2v_r^2\right) f(E,L)\,\mathrm{d}v_r\,\mathrm{d}v_\theta\,\mathrm{d}v_\phi} \tag{19}$$

By similar logic to the calculation of density we can say that:

$$1-\beta(r) = \frac{\int \left(\frac{L^2}{r^2}\right) f(E,L)\left(2\left[E - \Phi(r) - \frac{L^2}{2r^2}\right]\right)^{\frac{-1}{2}}\,\mathrm{d}L^2\,\mathrm{d}E}{\int \left(2v_r^2\right) f(E,L)\,\mathrm{d}E\,\mathrm{d}L^2} \tag{20}$$

As before we easily perform the integration over E and use the Heaviside functions to place limits on the integration over L^2 but the resulting expression is more complicated:

$$1-\beta(r) = \frac{\frac{1}{\sqrt{2}}\int_0^{L_{cut}^2}\left(\frac{L^2}{r^2}\right)\left(E_0 - \Phi(r) - \frac{L^2}{2r^2}\right)^{\frac{-1}{2}}\,\mathrm{d}L^2}{2\sqrt{2}\int_0^{L_{cut}^2}\left(E_0 - \Phi(r) - \frac{L^2}{2r^2}\right)^{\frac{1}{2}}\,\mathrm{d}L^2} = \frac{1}{4}\frac{\mathbb{I}_1}{\mathbb{I}_2} \tag{21}$$

For clarity we will solve each integral individually as they require substitutions to be easily soluble. We consider the numerator first and make a substitution of $Y = L^2/L_{cut}^2$ to make the problem dimensionless:

$$\begin{aligned}\mathbb{I}_1 &= \int_0^{L_{cut}^2} \frac{L^2}{r^2\sqrt{\left(E_0 - \Phi(r) - \frac{L^2}{2r^2}\right)}}\,\mathrm{d}L^2 \\ &= \frac{\left(L_{cut}^2\right)^2\sqrt{2}}{r\sqrt{L_{cut}^2}}\int_0^1 \frac{Y}{\sqrt{\left(\frac{2r^2}{L_{cut}^2}\left[E_0 - \Phi(r)\right] - Y\right)}}\,\mathrm{d}Y\end{aligned} \tag{22}$$

Similarly for the denominator we make the same substitution:

$$\begin{aligned}\mathbb{I}_2 &= 2\sqrt{2}\int_0^{L_{cut}^2}\sqrt{\left(E_0 - \Phi(r) - \frac{L^2}{2r^2}\right)}\,\mathrm{d}L^2 \\ &= \frac{2L_{cut}^2\sqrt{L_{cut}^2}}{r}\int_0^1\sqrt{\left(\frac{2r^2}{L_{cut}^2}\left[E_0 - \Phi(r)\right] - Y\right)}\,\mathrm{d}Y\end{aligned} \tag{23}$$

These integrals can be solved analytically and the result for β expressed as:

$$\beta = \frac{\sqrt{(1-x)}\left(\frac{3x}{2}\right)}{1-(1-x)^{\frac{3}{2}}} \text{ where } x = \frac{L_{cut}^2}{2r^2\left(E_0 - \Phi\right)} = \frac{L_{cut}^2}{r^2 v_c^2} \tag{24}$$

Similarly to the density profile, the anisotropy profile can produce imaginary results if $x > 1$ because $\frac{L_{cut}^2}{r^2} > \frac{L_{circ}^2}{r^2}$ at a particular radius. This, again, corresponds to regions of the system where all real orbits lie below the angular momentum threshold. Again, by analogy to taking taking the real part of the density, we avoid this by enforcing a maximum value of x:

$$\text{if } x > 1 \text{ then } x = 1$$

This limits the angular momentum threshold to the largest physically allowed angular momentum at radii where the imaginary numbers would otherwise be produced. This does not change the physical implications of the formula and just ensures mathematical consistency.

We can calculate σ_r^2 by using Eq. 18 and following a similar line of reasoning as for the anisotropy. Using the parameterisation from Eq. 24 yields:

$$\sigma_r^2 = \frac{2\left(E_0 - \Phi\right)\left[1 - (1-x)^{\frac{3}{2}}\right]}{9\left(1 - \sqrt{(1-x)}\right)} \tag{25}$$

The tangential dispersions can either be found by similarly or by combining the radial dispersion with the anisotropy. They wont be reproduced here as they are not used in our analyses.

3.3 Finding Potential

We can use Poisson's equation to find the potential by integrating the following second order ODE:

$$\frac{\mathrm{d}^2(r\Phi)}{4\pi G r \mathrm{d}r^2} = 4\sqrt{2}\pi A\left(\sqrt{E_0-\Phi}-\sqrt{E_0-\Phi-\frac{L_{cut}^2}{2r^2}}\right) \quad (26)$$

where, to be rigorous, we have included the dimensional prefactor A from our DF of Eq. 9.

This can be cast into a dimensionless form by the following scaling:

$$r = B\tilde{r};\ \Phi = E_0 - C\tilde{\Psi} \rightarrow \frac{\mathrm{d}\left(E_0-\tilde{\Psi}\right)}{\mathrm{d}\tilde{r}} \equiv -\frac{\mathrm{d}\tilde{\Psi}}{\mathrm{d}\tilde{r}};\ L^2 = B^2 C \tilde{L}^2 \quad (27)$$

where we require that $C = (AB^2G)^2$ for consistency.

This gives us the following dimensionless expression that requires solving:

$$-\frac{1}{4\pi\tilde{r}^2}\frac{\mathrm{d}}{\mathrm{d}\tilde{r}}\left(\tilde{r}^2\frac{\mathrm{d}\tilde{\Psi}}{\mathrm{d}\tilde{r}}\right) = 4\sqrt{2}\pi\left(\sqrt{\tilde{\Psi}}-\sqrt{\tilde{\Psi}-\frac{\tilde{L}_{cut}^2}{2\tilde{r}^2}}\right) = 4\sqrt{2}\pi\tilde{\rho}(\tilde{r}) \quad (28)$$

As with Eq. 16 we have an unphysical case for small r and large L_{cut}^2 which we resolve by taking only the real part of the root. To solve the ODE we apply initial conditions that:

$$\tilde{\Psi}(\tilde{r}=0) = (4\pi)^2;\ \frac{\mathrm{d}\tilde{\Psi}(\tilde{r}=0)}{\mathrm{d}\tilde{r}} = 0 \quad (29)$$

where the choice of the constant $(4\pi)^2$ is arbitrary and has been chosen here to make the radius of the system of order unity.

The equation must be solved numerically and the resulting $\tilde{\Psi}(r)$ is shown in Fig. 3.

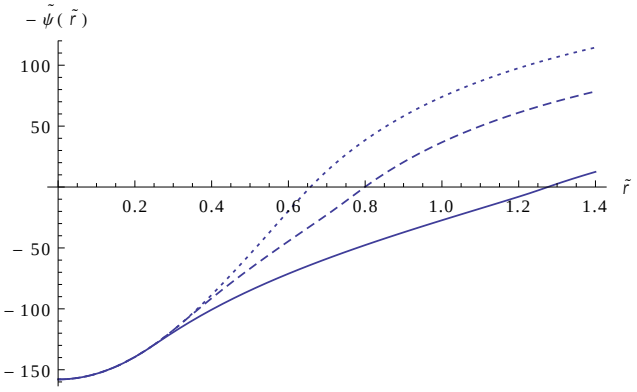

Figure 3. The numerically derived potential for our distribution function. The potential becomes positive at the point where $\tilde{\rho} = 0$. The potential is plotted for three models corresponding to $\xi = \{1, 1.5, 2\}$ (see Eq. 30) for the solid, dashed, and dotted lines respectively. Although $\tilde{\Psi}$ is decreasing faster than $\tilde{r}$ in the outer regions, it will behave like a Kepler potential at radii larger than the size of the system as the system is truncated at finite radius.

4 UNDERSTANDING THE SYSTEM

We have arrived at an analytically self-consistent system which should avoid the problems from section 2. We can summarise our system by collating our results so far:

$$\rho = 4\sqrt{2}\pi A\left(\sqrt{\Psi}-\sqrt{\Psi-\frac{L_{cut}^2}{2r^2}}\right)$$

$$\sigma_r^2 = \frac{2\left(E_0-\Phi\right)\left[1-(1-x)^{\frac{3}{2}}\right]}{9\left(1-\sqrt{(1-x)}\right)}$$

$$\beta = \frac{\sqrt{(1-x)}\left(\frac{3x}{2}\right)}{1-(1-x)^{\frac{3}{2}}} \text{ where } x = \frac{L_{cut}^2}{2r^2\left(E_0-\Phi\right)}$$

4.1 Characterising the density profile

We first of all note that our density profile is an 'augmented density' profile *i.e.* our density can be expressed only in terms of Ψ and r. However, unlike the augmented density functions used in the counter-examples of Van Hese et al. (2011), ours is not separable in terms of those variables. Our density function thus cannot be described using the basis set of separable augmented density functions that are used to construct their models, putting it in a different class.

The density at a given point can be thought of as the amount of orbits which require a particle to pass through that radius. As we established, our DF from Eq. 9 means that we are only allowing orbits with angular momentum $0 < L^2 < L_{cut}^2$ and energy $E = E_0$. It is convenient to equivalently think of the density as being *the sum of all possible, physical orbits of energy* E_0 *minus all orbits of energy* E_0 *and* $L^2 > L_{cut}^2$.

We can see this interpretation directly in Eq. 16 where the density is the difference between two terms which, as we will now discuss, correspond to the description above.

The first term, $\sqrt{E_0-\Phi}$, represents all physical orbits of energy E_0. As we can see from Fig. 3, the potential of the system is a monotonically increasing function.

The second term, $\sqrt{E_0-\Phi-\frac{L_{cut}^2}{2r^2}}$, is more complex due to the addition of an angular momentum term. This represents all orbits of energy E_0 and an angular momentum L_{cut}^2.

In Fig. 3, and in most subsequent figures, we plot a handful of models with different values of $\tilde{L}_{cut}^2$ as this is key parameter which determines the behaviour of the model. The models are generated by:

$$\tilde{L}_{cut}^2 = 14.37\xi \quad (30)$$

where ξ is a free parameter, and 14.37 was chosen to give an arbitrary but convenient value for $\tilde{L}_{cut}^2(\xi = 1)$ and is related to $\tilde{\Psi}(\tilde{r} = 0)$. As we can see from this figure, increasing $\tilde{L}_{cut}^2$ will decrease the radius of the system. To allow for better comparison of models we normalise the radius of each model in subsequent figures.

So, as we see from Fig. 4, we have two components for the density and have arranged them such that the number of allowed orbits is proportional to the area under the curve. The area under the largest curve contains all orbits given by $\sqrt{E_0-\Phi}$ and any angular momentum. The area under the smaller curve is given by $\sqrt{E_0-\Phi-\frac{L_{cut}^2}{2r^2}}$ which only

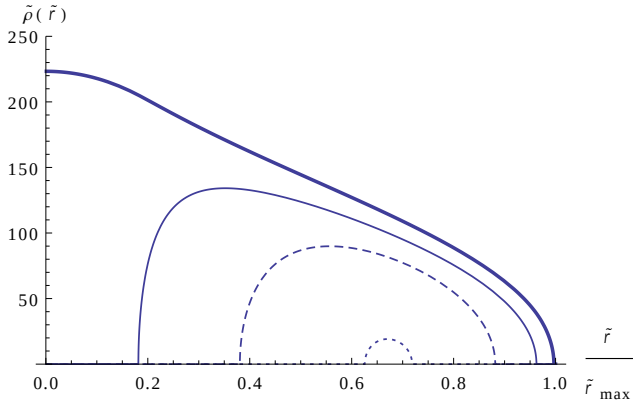

Figure 4. Both components of the density in our example model. The area under the largest curve (thick, solid line) contains all physical orbits in the system while the smaller curves (solid, dashed and dotted) contain all allowed orbits that have L^2 *greater* than L^2_{cut} for $\xi = \{1, 1.5, 2\}$ (see Eq. 30).

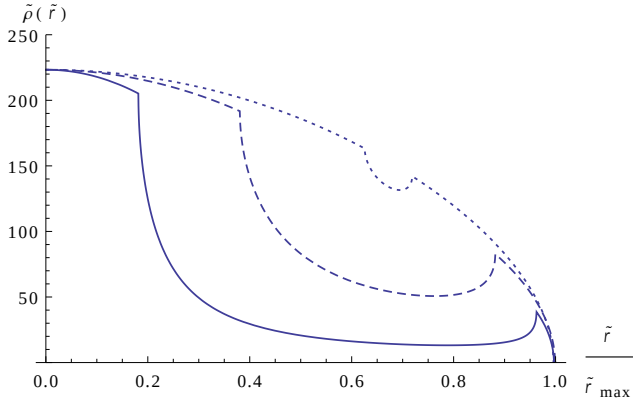

Figure 5. The full density profile for our distribution function. The density is plotted for three models corresponding to $\xi = \{1, 1.5, 2\}$ (see Eq. 30) for the solid, dashed, and dotted lines respectively. Significant violation of the GDSAI is expected to occur in the sharp peak at large radii.

contains orbits with angular momentum *greater* than L^2_{cut} for several different values of the threshold.

We recall that our overall density is the difference between these two components, which produces Fig. 5. The immediate feature of note is the sharp peak towards the outer edge which is the feature that makes this system so useful.

Now that we understand how this profile is formed we explain why these features arise. Bear in mind that this is a mono-energy system and that all orbits have total energy of E_0.

At small radii, our angular momentum constraint has minimal impact. The small value of r means that even a highly circular orbit will have an angular momentum that is under the L^2_{cut} threshold. Thus we find there is a large number of possible orbits and the density is high.

As we move further out an orbit of given circularity will have higher angular momentum so allowed orbits are progressively more radially anisotropic in order to fit under the

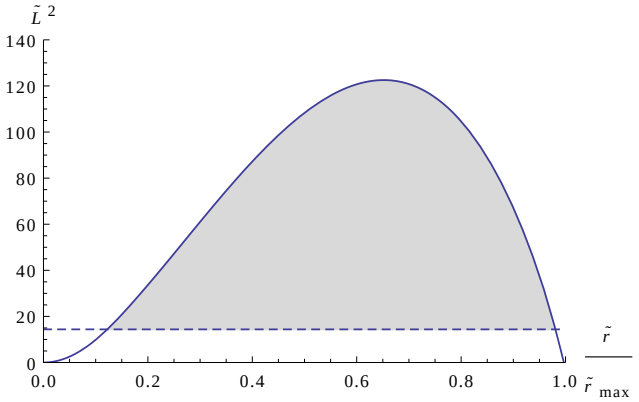

Figure 6. Variation of the maximum possible angular momentum, $\tilde{L}^2_{max}(\tilde{r})$, with radius showing that at large and small radii it is impossible for a particle of energy E_0 to surpass the angular momentum cutoff. The cutoff $\tilde{L}^2_{cut}(\xi = 1)$ is indicated by the horizontal line with the shaded region representing otherwise permissible orbits that will fail the angular momentum cut. $\tilde{L}^2_{max}$ was found by using Eq. 31.

angular momentum limit. Accordingly, fewer allowed orbits exist at these radii and fewer particles found than expected.

Finally, in the outermost regions the angular momentum limit no longer has any impact. Although the radius is large, the angular momentum of a circular orbit here is very low as a lot of the particle's energy is used to overcome the potential. This means very little is left to be used for kinetic energy and thus the tangential velocity is extremely small. Even a completely circular orbit at this radius will have an angular momentum below the threshold. Using the same logic as for small radii this means that the density will be a little higher than at smaller radii. This can be seen in Fig. 6.

The last feature to understand is the sharp rise in the density at large radii. This is difficult to discuss analytically due to the lack of an analytical solution to the potential. For example, if we try to understand how the angular momentum of a perfectly circular orbit changes with radius we would rearrange Eq. 12 for the case where $v_r = 0$:

$$L^2_{max} = 2r^2\Psi(r) \tag{31}$$

Since we do not know the dependence of Ψ on r we cannot construct analytical expressions for the slope. Thus, to understand the reason for the increase in density we must rely on the figures and numerical results.

At the point where the density rises, we can see from Fig. 6 that L^2_{max} is decreasing rapidly. This means that, as the radius increases, a particle can be on a increasingly circular orbit and still be under the angular momentum threshold. In other words, a particle is allowed to make a larger angle between the radial axis and its velocity vector the further it is from the centre. This also means that the amount of orbital configurations possible at these radii *i.e.* the phase-space density, is increasing in proportion.

In the absence of an angular momentum limit then, as seen in Fig. 4, the density naturally decreases monotonically as the potential increases towards the edge of the system. However, comparing these two figures shows that the rate of

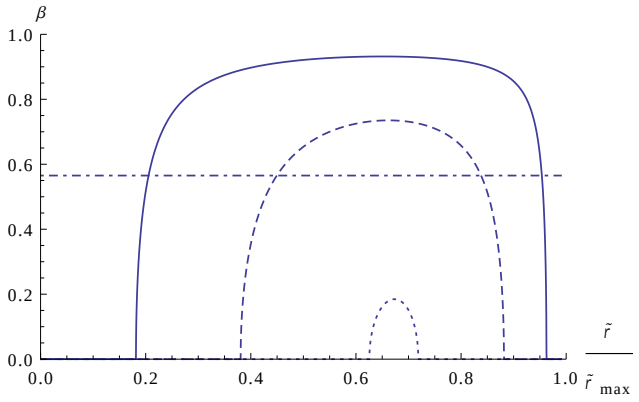

Figure 7. The anisotropy profile for our system demonstrating the isotropic core and edge regions for the three models $\xi = \{1, 1.5, 2\}$ (the solid, dashed, and dotted curves). The dot-dashed line represents the anisotropy corresponding to the nominal radial orbit instability threshold of $2\bar{T}_r/\bar{T}_t \approx 2.3$ (Merritt & Aguilar 1985).

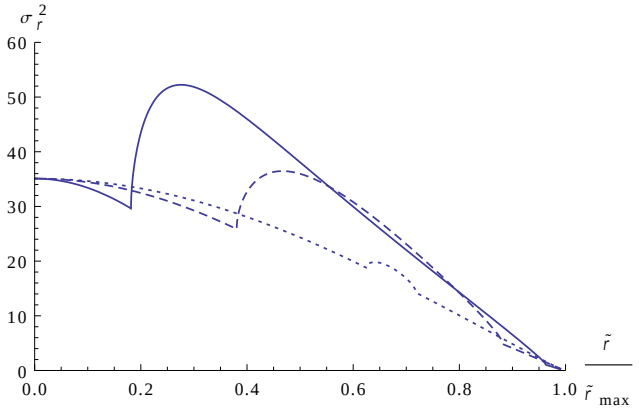

Figure 8. The radial velocity dispersion profile of our system for the three models $\xi = \{1, 1.5, 2\}$ (the solid, dashed, and dotted curves). Upon entering or leaving regions of the model where the angular momentum cut is removing orbits there is a discontinuity as there is a abrupt decrease in the amount of energy that can be used in tangential motion.

decline in phase-space density due to the potential is *smaller* than the rate of *increase* due to the range of allowed angles velocity vectors.

This means that over a small range of radii the phase-space density and, correspondingly, the mass density increases until all orbits fall under the angular momentum threshold again. At this point the system has no orbits left to be added to the density as the radius increases because none are being excluded. Accordingly the decline in density resumes until the edge of the system.

4.2 Characterising the anisotropy profile

One key feature of this model is that, unlike the models in Van Hese et al. (2011), it has very low core anisotropy. In fact it is isotropic at both small and large radii, and is only radially anisotropic for a set of intermediate radii as can be seen in Fig. 7.

As discussed in previous sections, the angular momentum threshold removes no orbits from the core of the system or the outskirts. This is because even circular orbits at these radii have low angular momentum due to either the small radius of the orbit or the low tangential velocity of the particle. At these radii the angular momentum function of our DF, $H\left(L_{cut}^2 - L^2\right)$, is equal to 1 for all orbits and thus the DF overall is a function only of energy. This means that all energy is necessarily split evenly between velocity components and that region is isotropic (Binney & Tremaine 2008).

In the regions where the angular momentum limit is removing orbits, the change in anisotropy can be thought of thusly. Imagine trying to construct a particle on an orbit that tries to maximise its angular momentum by minimising its radial velocity component, as we did when constructing Eq. 31. Since this orbit must have a certain amount of energy it has a very predictable angular momentum which will put the particle over the L_{max}^2 threshold. This means that this orbit, and all highly tangential ones, are removed, leaving only the more radial ones. Given that the system would be isotropic if not for this process, we can say that any radii where the angular momentum cut removes orbits will be radially anisotropic.

This behaviour is shown directly by looking again at Fig. 6. The shaded orbits above the angular momentum threshold $\tilde{L}_{cut}^2$ are excluded which implies that any radii with a shaded portion of the curve will be radially anisotropic. The amount of anisotropy will grow with the size of the shaded area.

Because the transition between the isotropic regions and the anisotropic regions is a sharp, when we examine the individual components of velocity dispersion we see discontinuities. Fig. 8 shows how the slow decrease of energy in radial velocity is suddenly reversed upon reaching the anisotropic regions of the system. A smaller discontinuity is also present upon reaching the isotropic regions at large radii. These correspond to the two discontinuities in the density profile.

4.3 Violation of the GDSAI

We can now confirm that our system includes violation of the GDSAI at certain radii. We have proved that our system is radially anisotropic in the regions where the angular momentum threshold is removing orbits. We have also demonstrated that our system's density profile flattens or rises in those same regions due to the exclusion of a region of phase-space. From this we can see that we have two regions where we would expect to find that $\gamma < 2\beta$ and thus violate the GDSAI.

At the radii immediately prior to the density peak we will see significant violation as the density is *rising* sharply with radius and so $\gamma < 0$. However, we also find less severe violation at a large range of intermediate radii where the density profile is extremely flat and thus $\gamma \approx 0$. Since the anisotropy is high at these radii, the system can be configured such that $\gamma < 2\beta$ at these radii as well.

The degree of violation exhibited by our system is plotted in Fig. 9 where we show curves of γ and 2β for the model $\xi = 1$. Any radius where $\gamma < 2\beta$ is violating the GDSAI. We can see that approximately 2/3 of radii in this model display such behaviour, corresponding to 16% of the model's mass.

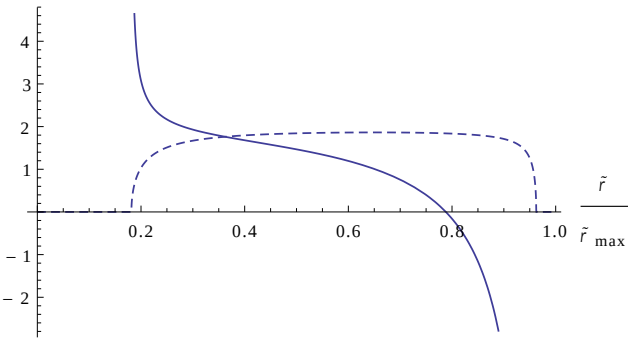

Figure 9. Showing both γ and 2β as functions of radius for the model $\xi = 1$. The point where the lines cross represents the beginning of the regions that violate the GDSAI.

Accordingly, we find that our system can produced from a globally positive DF, have a low core anisotropy, and still significantly violate the GDSAI.

Having demonstrated the theoretical interest of our system, we will now discuss the stability of our solution.

5 SYSTEM STABILITY

5.1 Radial Instability

A fundamental measure of radial stability is the anisotropic extension of the Doremus-Feix-Baumann theorem (Doremus et al. 1971, 1973; Gillon et al. 1976; Binney & Tremaine 2008) which states that a stable system must satisfy $\mathrm{d}f_0/\mathrm{d}H_0 < 0$. For our DF this requires that $\mathrm{d}f(E)/\mathrm{d}E < 0$ which is problematic because $f(E) = \delta(E_0 - E)$ and, due to the peculiarities of the Dirac delta, its derivative is formally undefined. However, since this is also a necessary criteria for the emergence of the Hénon Instability (Barnes et al. 1986; Merritt 1999) we can use the Hénon criteria as an indicator of radial instability.

5.2 Hénon Instability

A very similar system that underwent extensive stability testing is the $n = 1/2$ polytrope. The testing of Hénon (1973) and Barnes et al. (1986) demonstrated that the oscillatory stability of the polytrope was due a uneven radial velocity distribution that was termed the 'Hénon Instability'. It is worth noting that the GDSAI counter-examples of Van Hese et al. (2011) were unstable according to the Hénon criteria.

The Hénon instability will appear in our systems if they possess two or more distinct peaks in the radial velocity distribution $P(v_r)$ where:

$$P(v_r) = \iint_{-\infty}^{+\infty} \delta\left(E - E_0\right) H\left(L_{cut}^2 - L^2\right) \mathrm{d}v_\theta \mathrm{d}v_\phi$$
$$= H\left(\frac{1}{2}v_r^2 - \Psi(r) + \frac{L_{cut}^2}{2r^2}\right) - H\left(\frac{1}{2}v_r^2 - \Psi(r)\right) \tag{32}$$

This distribution will, after being normalised, give us a probability density that is constant over a narrow range of radial velocities:

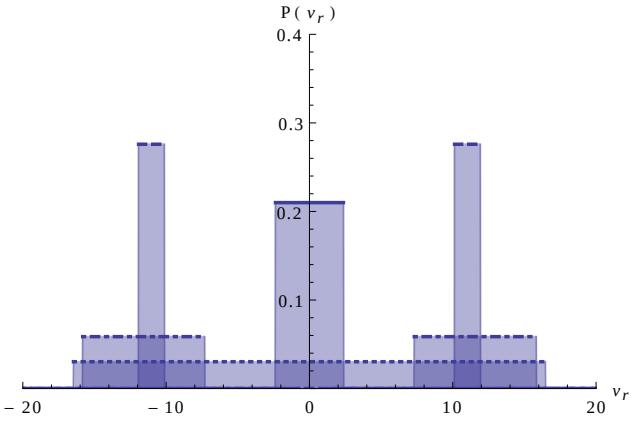

Figure 10. A probability distribution bar plot showing the normalised probability of finding a particle with a given radial velocity at certain radii. Bars topped with a dotted, dot-dashed, dashed, and solid line represent the probabilities at $\tilde{r} = \{0.22, 0.27, 0.6, 1.25\}$ respectively.

$$P(v_r) \neq 0 \text{ where } \frac{-L_{cut}^2}{2r^2} < \frac{1}{2}v_r^2 - \Psi(r) < 0 \tag{33}$$

From this, and our intuition about the allowed orbits, we can explain the distribution seen for a selection of radii in the model $\xi = 1$ in Fig. 10.

At small radii, $\frac{-\tilde{L}_{cut}^2}{2\tilde{r}^2} \ll 0$ so the only constraint on v_r is energy conservation. Thus we expect a range of velocities out to some maximum value.

At intermediate radii a particle is not allowed to have negligible radial velocity. If a particle here has $v_r \approx 0$ then the mono-energy rule would demand that it compensate with significant v_t which, at these radii, would put it over the $\tilde{L}_{cut}^2$ threshold. Accordingly, the radial velocity distribution at these radii will be two sharp peaks with a gap around $v_r = 0$. The width of the peaks is determined by $\tilde{L}_{cut}^2$ and the radius.

Finally, at the outer edge of the system the angular momentum threshold no longer removes orbits and so particles with $v_r \approx 0$ are allowed once again. The two peaks reform into a single peak centred around $v_r = 0$ like at small radii but with a smaller width due to the much smaller amount of kinetic energy possessed by particles at these radii.

Since our models clearly possess two very sharp and well-defined peaks at most radii we conclude that this model may be susceptible to the Hénon instability.

5.3 Radial Orbit Instability

The stability of our system to non-radial modes is easier to assess. We use the simple stability measure of $2\bar{T}_r/\bar{T}_t$ which has been the subject of much debate (Merritt 1999). Looking back at Fig. 7 we see that the model $\xi = 1$ is over the limit throughout most of the system. However, models with a higher angular momentum threshold can consistently have low enough anisotropy to avoid the instability.

This is shown in Fig. 11 where compliance with the radial orbit instability criteria is plotted against the angular

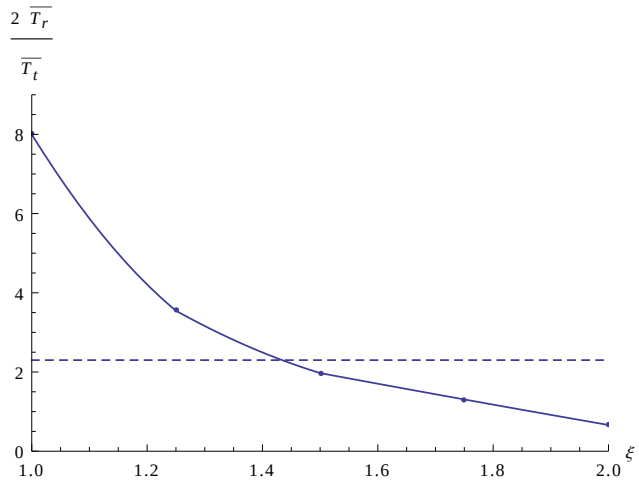

Figure 11. The dependence of $2T_r/T_t$ against the ξ of the model. The radial orbit instability criteria of $2T_r/T_t \approx 2.3$ is marked with a dashed line for clarity. The stability of the model depends on ξ with larger values producing more stable systems.

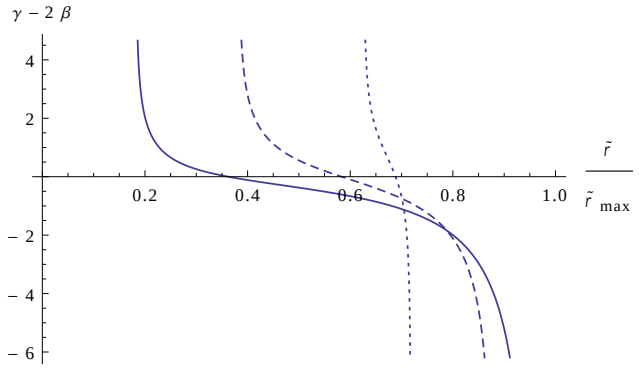

Figure 12. The violation of the GDSAI as a function of radius for the three models $\xi = \{1, 1.5, 2\}$ (the solid, dashed, and dotted curves). The vertical axis does not extend to show the curves at all radii in order to clearly see the radii at which they violate the GDSAI. Models with small ξ will never violate the GDSAI everywhere, only across a larger range of range. In our models $\gamma - 2\beta > 0$ is always true at $r = 0$.

momentum threshold. Models with $\xi \approx 1.45$ and above appear to be stable. So, it appears that the stability of the system is a function of the parameter ξ.

5.4 Stability Dependence on L^2_{cut}

We have seen how our system has the potential to suffer from a variety of stability problems. However, there is reason to believe that the degree of instability can be controlled, if not mitigated entirely.

We begin by once again noting that, in regions of our system where L^2_{cut} is higher than the largest possible angular momentum (see Fig. 6), our system behaves as if the DF is exclusively a function of energy and is thus isotropic. Additionally, we consider that L^2_{cut} is a tunable parameter through Eq. 30.

In Fig. 12 we can see that if we raise L^2_{cut} then it affects less of the system which, in turn, will become increasingly isotropic. Importantly, both the Hénon and radial orbit instabilities are diagnosed by considering the ratio or allowed domain of velocity components. Therefore, if a system is isotropic, then it is guaranteed to be stable to both of these effects. This is what we see in Fig. 11.

Accordingly, it is the case that the higher L^2_{cut} is set, the more of the system will be isotropic, and the more of the system will pass those stability criteria. This implies that *the stability of the system is exclusively dependent on the value of the freely tunable parameter* L^2_{cut}. The only limits are the cases of an exactly radial system of infinitesimal density and a completely isotropic system *i.e.* $0 < L^2_{cut} \leqslant Max\left(L^2_{max}(r)\right)$.

Thus, one can construct a system using this DF that violates the GDSAI to specific degree over a specific set of radii by choosing a large enough value for L^2_{cut}. It thus follows that a system could be constructed which produces a small degree of violation over such a small range of radii that it would only be susceptible to the Hénon and radial orbit instabilities to a vanishingly small degree. It is thus true to say that the stability implications thus become negligible as $L^2_{cut} \to Max\left(L^2_{max}(r)\right)$.

This is particularly true for the Radial Orbit Instability criteria as the susceptibility is averaged over the entire system. Additionally, the Hénon criteria is only necessary, not sufficient, for instability (Merritt 1999) and it is thus difficult to claim that small, highly local violations of the criteria represent chronic instability in the model.

This is seen clearly if the GDSAI is plotted for a selection of our models. In Fig. 12 we can see the impact of changing ξ on our models. Regions where the curve passes below the vertical axis indicates violation of the GDSAI. In particular, we have shown that the model where $\xi = 2$ is stable against radial orbit instability and now can see that it violates the GDSAI across a small range of radii. In particular, the violation at large radii is significant.

The DF of that model is positive, the majority of the system is isotropic, and the violation of the GDSAI is severe. The only problem with the system is that its stability cannot be rigorously guaranteed. We believe that this proves that the slope-anisotropy inequality cannot be extended as a global measure of DF positivity and that stability arguments still present the best tools for judging a collisionless system.

6 GENERALISING THE MODEL

The problems with instability cannot be resolved by using a mono-energy DF. Remember that we established that our systems can violate the GDSAI by excluding high angular momentum orbits to create a density plateau and radial anisotropy. If this is the case then we can generally describe the DF as a mono-energy halo of energy E_1:

$$DF = \delta(E_1 - E) f\left(L^2\right) \tag{34}$$

where we require that $f(L^2)$ decreases as L^2 rises. This is how the model will favour low angular momentum orbits.

We can then use this DF to find a general expression for the probability distribution of radial velocities as required for an analysis of the Hénon instability (see §5.2).

$$P(v_r, r) = 2\pi \int \delta\left(E_1 - \Phi(r) - \frac{v_r^2}{2} - \frac{v_t^2}{2}\right) f\left(v_t^2 r^2\right) \mathrm{d}\left(\frac{v_t^2}{2}\right) \tag{35}$$

This then gives a general solution:

$$\begin{aligned} P(v_r, r) &= f\left(v_t^2 r^2\right)\Big|_{\frac{v_t^2}{2} = E_1 - \Phi(r) - \frac{v_r^2}{2}} \\ &= f\left(\left(2E_1 - 2\Phi - v_r^2\right) r^2\right) \end{aligned} \tag{36}$$

Now, we specified that $f(x)$ is a function which decreases as its argument increases. This means that for a fixed radius r, $f\left(\left(2E_1 - 2\Phi - v_r^2\right) r^2\right)$ is an increasing function of v_r.

This has the unfortunate implication that $f(v_r = 0) < f(v_r > 0)$. In other words the velocity distribution will always have a trough at $v_r = 0$ and two peaks at $v_r = \pm\sqrt{2E_1 - 2\Phi}$ meaning the Hénon instability is always going to cause problems for models of this kind.

To try and avoid this the model can be extended and generalised further. Our generalised DF is of the form:

$$f(E, L) = A\left[H(E - E_1) - H(E - E_2)\right] H\left(L_{cut}^2 - L^2\right) g(E) \tag{37}$$

where $g(E)$ is a function of energy and $E_1 < E_2 \leqslant 0$ are constant values for energy. With this DF, we allow orbits in the system that have angular momentum $L^2 < L_{cut}^2$, energies of $E_1 < E < E_2$ and the function $g(E)$ is left free. We can see that the DF of Eq. 9 can be approximated by the special cases where $E_1 \to E_2$ and $g(E)$ is constant.

For the purposes of illustration we will use $g(E) = e^{-BE}$ if specific examples or figures are needed. The corresponding density function for this illustrative model is:

$$\begin{aligned} \rho = \Bigg\{ & 4\pi\sqrt{2}B^{-1.5} \\ & \Big[e^{-B\Phi}\left[\Gamma(1.5, B(E_1 - \Phi)) - \Gamma(1.5, B(E_2 - \Phi))\right] \\ & e^{-B\left(\Phi + \frac{L_{cut}^2}{2r^2}\right)}\left[\Gamma(1.5, B\mathcal{E}_1) - \Gamma(1.5, B\mathcal{E}_2)\right]\Big]\Bigg\} \\ & \text{where } \mathcal{E}_n = E_n - \Phi - \tfrac{L_{cut}^2}{2r^2} \end{aligned} \tag{38}$$

where B is a constant and $\Gamma(a, x)$ is the incomplete Gamma function (Hazewinkel 1994) which is defined as:

$$\Gamma(a, x) = \int_x^\infty t^{a-1} e^{-t} \mathrm{d}t \tag{39}$$

The corresponding potential is numerically derived and the other system characteristics are computed using the same methods as in §3. The analytical formulae are not given here as they are prohibitively large and the model is only for illustration.

This generalised DF is still capable of violating the attractor for the same reasons that allowed the more specific case to do so. For example, in the density peak of Fig. 5 we have a transition domain where $\gamma \ll 0$ while the anisotropy profile is similarly making a transition from strongly radially anisotropy to isotropy as discussed in detail in §4. This behaviour remains unchanged in the generalised DF as the angular momentum limit can be set so that it removes *all* circular orbits at intermediate radii, making the system underdense and anisotropic. Again, since this cut *only* removes highly circular orbits it can *only* make the system more radially anisotropic at these radii. Thus, the violating behaviour is still seen in our generalised system when the density peak is produced as the system moves out of the underdense domain and towards isotropy.

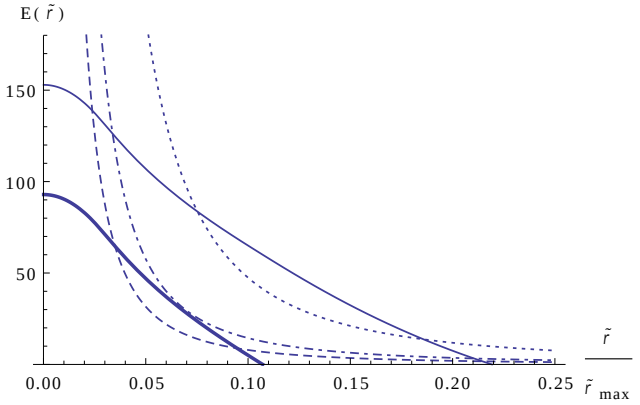

Figure 13. Plots of important energies for the illustrative model of Eq. 38 where $E_1 = -70$, $E_2 = -10$, $B = 0.0005$, and $K = 4\pi$. The solid and thicker solid curves are $E_1 - \Phi$ and $E_2 - \Phi$. Other curves are $L_{cut}^2/2r^2$ for different values of L_{cut}^2. The dashed line is for a harsh cut of $L_{cut}^2 = 0.012566$. The dot-dashed line is $L_{cut}^2 = 0.022934$ which only touches $E_1 - \Phi$. The dotted curve is $L_{cut}^2 = 0.075398$ which only excludes a very small amount of orbits.

Accordingly, violation in this region can be caused by simply setting $L_{cut}^2 \leqslant 2R^2(E_1 - \Phi)$ where R is some chosen intermediate radius at which the angular momentum of circular orbits in the system is maximised. This causes the angular momentum cut to exclude all circular orbits down to the ones of lowest allowed energy as shown in Fig. 13. Note that, as demonstrated in Fig. 12, the violation will actually begin at smaller radii due to the gradual flattening of the density profile occurring alongside the rise in anisotropy. However, the exact point at which this takes place will be very model dependent.

The problem remains that, as discussed in §5.2, removing all highly circular orbits implies that $P(v_r \approx 0) = 0$ which leads to the sharply double-peaked velocity profiles that are indicative of the Hénon instability. So, if we set a harsh angular momentum limit then we can remove a large number of circular orbits, create our peak and anisotropy to violate the GDSAI as before, but at the cost of stability. Conversely, if we remove the limit entirely then the system becomes isotropic and smooth, but fails to violate the inequality. However, while these were the only options for the original DF, the new DF allows intermediate cases which can give us some insight as shown in Figs. 14 and 13.

We examine the case where $L_{cut}^2 = 2r^2(E_1 - \Phi)$ has a single solution, compared to the usual two, as shown in Fig. 13. In this instance the angular momentum limit only excludes orbits down to the orbit of lowest energy which is completely circular. In other words, if the limit was raised infinitesimally then it would just be possible to have an ex-

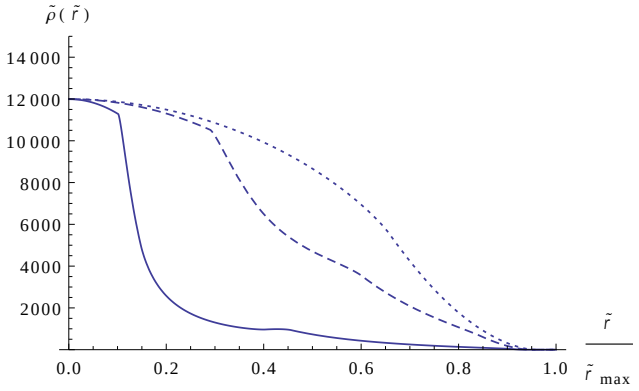

Figure 14. The density models of the systems in Fig. 13. The systems are all $E_1 = -70$, $E_2 = -10$, $B = 0.0005$, and $K = 4\pi$ where the dashed line is $L^2_{cut} = 0.012566$, the dot-dashed line is $L^2_{cut} = 0.022934$, and the dotted curve is $L^2_{cut} = 0.075398$. Note the bump at intermediate radii rather than the sharp peaks seen in previous models as well as the difficulty in getting a positive gradient.

actly circular orbit with exactly $E = E_1 - \Phi(R)$ at a radius R which maximised that orbit's angular momentum. What we see in Fig. 14 is that already the model is not excluding enough orbits to force a local $\gamma < 0$, which is the feature in our models which always guarantees a violation, but this is only the first case where $P(v_r = 0) \neq 0$ for all energies. In other words this case is still Hénon unstable because $P(v_r = 0) \ll P(v_r > 0)$ but is *already* unlikely to produce the violation due to $\gamma > 0$ and an anisotropy that will not be as high as in models with harsher angular momentum cuts.

This is true of every model where $2r^2(E_1 - \Phi) \ll L^2_{cut} < 2r^2(E_2 - \Phi)$. As the number of circular orbits allowed increases, it follows that γ must rise, $\beta \to 0$, and $P(v_r = 0)$ will also rise. However the probability of very low v_r *will* still be reduced compared to a system where no orbits are removed. In other words, the instability will be present over some range of radii if the angular momentum threshold excludes any orbits at all.

Between these cases we see the behaviour of our generalised model is comparable to that of our simpler, more specific DF. Depending on the choice of parameters, the system can violate the GDSAI over a range of radii, however achieving such a violation decreases the chance of finding particles with low v_r. Cutting a large amount of orbits can guarantee violation at the cost of severe instabilities where $P(v_r \approx 0) = 0$, while weaker cuts causes milder instability where $P(v_r \approx 0) \neq 0$ and may fail to achieve violation at all.

This line of reasoning leads us to the conclusion that while any suitable combination of parameters can violate the GDSAI at different radii and to a different degree, the underlying mechanism of removing high angular momentum orbits is never going to produce a model that is stable under the Hénon criteria.

7 SUMMARY

We have managed to construct an equilibrium system from a globally positive DF and low core anisotropy that violates the GDSAI. The magnitude of the violation is dependent on the value of the angular momentum threshold L^2_{cut}, which is also the parameter that controls the stability of the model. It is possible to pick values of this parameter where the majority of the system violates the GDSAI but is also unstable, or where the violation is highly local and the instability is negligible. This is a significant expansion on previous work showing that the GDSAI is not a universal law (Van Hese et al. 2011).

We conclude this shows that whether or not a system obeys the GDSAI does not constitute proof of the positivity or otherwise of the system's DF. Instead it seems more likely that the GDSAI is based more fundamentally on arguments of stability and only represents a 'soft constraint' on the DF through implicit connections to stability criteria. This is evidenced by the direct connection between local violations of the GDSAI and local instability, although it should be noted that the radial stability of our model is difficult to directly assess.

Exploring generalisations of the simple system have shown that this approach will not be able to yield a system that is stable under the Hénon criteria. Future work will therefore focus on mechanisms beyond the simple removal of very circular orbits.

In conclusion, we feel that while the GDSAI remains a useful guide, it should not be considered a definitive criterion in discussions of DF positivity.

8 ACKNOWLEDGEMENTS

The authors would like to thank Steen Hansen of the Dark Cosmology Centre for his helpful discussions and insight. Thanks also to Xufen Wu for her help and input.

REFERENCES

An J. H., Evans N. W., 2006, The Astrophysical Journal, 642, 752

Barnes J., Hut P., Goodman J., 1986, The Astrophysical Journal, 300, 112

Binney J., Tremaine S., 2008, Galactic Dynamics, second edition edn. Princeton University Press

Ciotti L., Morganti L., 2009, Monthly Notices of the Royal Astronomical Society, 393, 179

Ciotti L., Morganti L., 2010, Monthly Notices of the Royal Astronomical Society, 408, 1070

Ciotti L., Pellegrini S., 1992, Monthly Notices of the Royal Astronomical Society, 255, 561

Clowe D., Bradač M., Gonzalez A., Markevitch M., Randall S., Jones C., Zaritsky D., 2006, The Astrophysical Journal Letters, 648, L109

Cuddeford P., 1991, Monthly Notices of the Royal Astronomical Society, 253, 414

Doremus J. P., Baumann G., Feix M. R., 1973, Astronomy and Astrophysics, 29, 401

Doremus J. P., Feix M. R., Baumann G., 1971, Physical Review Letters, 26, 725

Gillon D., Cantus M., Doremus J. P., Baumann G., 1976, Astronomy and Astrophysics, 50, 467
Hansen S. H., 2004, Monthly Notices of the Royal Astronomical Society, 352, L41
Hazewinkel M., 1994, Encyclopedia of Mathematics (set). Kluwer
Hénon M., 1973, Astronomy and Astrophysics, 24, 229
Hernquist L., 1990, Astrophysical Journal
Komatsu E., Dunkley J., Nolta M., Bennett C., Gold B., Hinshaw G., Jarosik N., Larson D., Limon M., Page L., Spergel D., Halpern M., Hill R., Kogut A., Meyer S., Tucker G., Weiland J., Wollack E., Wright E., 2009, The Astrophysical Journal Supplement Series, 180, 330
Merritt D., 1999, Publications of the Astronomical Society of the Pacific, 111, pp. 129
Merritt D., Aguilar L. A., 1985, Monthly Notices of the Royal Astronomical Society, 217, 787
Navarro J., Frenk C., White S., 1996, The Astrophysical Journal, p. 255
Osipkov L. P., 1979, Pis'ma Astr. Zh., 5, 77
Polyachenko E. V., Polyachenko V. L., Shukhman I. G., 2013, Monthly Notices of the Royal Astronomical Society, 434, 3208
Taylor J., Navarro J., 2001, The Astrophysical Journal, 563, 483
Van Hese E., Baes M., Dejonghe H., 2011, The Astrophysical Journal, 726, 80
Zhao H., 1996, Monthly Notices of the Royal Astronomical Society, 278, 488

This paper has been typeset from a TEX/ LATEX file prepared by the author.